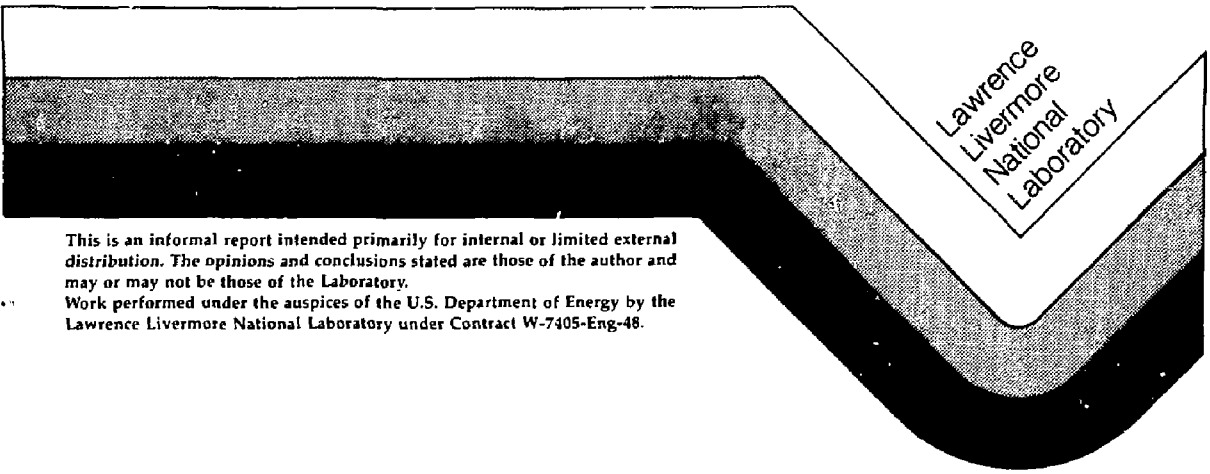UCID- 21329

The DIII-D Summary Contribution to the Final INTOR Workshop

D. N. Hill, S. L. Allen, N. H. Brooks, D. Content,
J. C. DeBoo, P. Gohil, G. Haas, D. Heifetz, C. L. Hsieh,
R. A. Hulse, G. L. Jackson, L. Lao, M. A. Mahdavi,
M. J. Mayberry, N. Ohyabu, D. E. Perkins, M. E. Perry,
T. W. Petrie, M. E. Rensink, T. Scoville, M. Shimada,
R. T. Snider, R. E. Stockdale, and R. D. Wood

February 26, 1988

Lawrence
Livermore
National
Laboratory

DISCLAIMER

THE DIII–D SUMMARY CONTRIBUTION
TO THE FINAL INTOR WORKSHOP

D.N. Hill, S.L. Allen, N.H. Brooks,[a] D. Content,[b] J.C. DeBoo,[a]

P. Gohil,[a] G. Haas,[c] D. Heifetz,[d] C.L. Hsieh,[a] R.A. Hulse,[d]

G.L. Jackson,[a] L. Lao,[a] M.A. Mahdavi,[a] M.J. Mayberry,[a] N. Ohyabu,[a]

D.E. Perkins, M.E. Perry,[b] T.W. Petrie,[a] M.E. Rensink,

T. Scoville,[a] M. Shimada,[c] R.T. Snider,[a] R.E. Stockdale,[a] AND R. Wood

Introduction and Summary

Impurities must be controlled in high temperature tokamak plasmas because the impurity radiation can limit the plasma temperature to values below that required for ignition. Impurity influx can be reduced with the use of the magnetic divertor configuration, which surrounds the hot dense plasma with a much cooler plasma that contacts material walls only on open field lines. Many present day tokamaks, such as ASDEX, DIII-D, JET, and JFT-2M routinely operate with divertor plasmas, and as a result have obtained the H-mode with its good energy confinement.

In DIII-D, good H-mode confinement $[\tau_E(NBI) = \tau_E(OH) \simeq 120$–$150$ ms at $I_p = 1$ MA] has been obtained [1,2] with up to 6 MW of neutral-beam injection (NBI). In this report we summarize the essential features of divertor operation for DIII–D H-mode plasmas. Briefly, our measurements show that:

(1) Large edge density and temperature gradients are obtained with scale lengths of a few cm at the midplane.

(2) In the steady state, approximately 10-20% of the input power is deposited on the divertor plates in a region that is peaked on the separatrix and extends radially over $\simeq 2$–4 cm at the outboard intercept. More power (2:1) reaches the outboard intercept than the inboard.

[a] *GA Technologies Inc.*

[b] *Johns Hopkins University*

[c] *Max-Planck-Institut für Plasmaphysik*

[d] *Princeton Plasma Physics Laboratory*

[e] *Japan Atomic Energy Research Institute*

(3) Low electron temperature (≤ 20 eV) and high density ($n_e^{div} \simeq n_e^{main} \geq 3\text{--}10 \times 10^{19}$ m^{-3}) at the divertor plates indicate that DIII-D obtains a high-recycling divertor during H-mode. DEGAS neutral transport modeling is consistent with these results.

(4) The duration of good H-mode confinement is limited by Edge Localized Modes (ELMs) rather than increasing impurity radiation.

(5) The dominant impurities, C and Ni, are concentrated in the edge plasma ($r/a \geq 0.5$) for $I_p \geq 1$ MA.

(6) Global impurity concentrations fall markedly with increasing plasma current.

The remainder of this report is outlined as follows. Section I contains a brief description of the DIII-D tokamak and the relevant diagnostics. Section II summarizes the divertor plasma parameters obtained during the H-mode and describes the heat loads on the divertor target plates. Section III presents the results of measurements of the central radiation and impurity content using data from an EUV spectrometer and a 21 channel bolometer array. Section IV concludes with a discussion of the implication of these results for the CIT and ITER tokamak designs.

I. Device Configuration

The single null, open divertor plasma configuration of DIII-D is shown in Fig. 1, which includes a cross section of the vacuum vessel and the MHD equilibrium magnetic flux surfaces for a typical H-mode discharge. The location of the flux surfaces was determined using the magnetic fitting code EFITD. In the usual case, the X-point is positioned 15–20 cm above the target plates and a gap of 3–5 cm between the separatrix and the main limiter is maintained by active feedback control. Below the X-point, the two legs of the separatrix intersect the vessel floor at an angle of about 45°, at which point the flux surfaces have expanded a factor of 3.5 on the outboard side and 7 at the inboard intercept relative to that at the midplane. At the target plates the angle of the actual field lines relative to the graphite tiles depends upon q, but is usually a shallow angle of less than 3° owing to $B_T \gg B_p$.

The interior walls of DIII-D are Inconel, and 15 m^2 of the 76 m^2 of the wall surface are covered with graphite. Approximately one-third of the graphite is used

for the divertor target plates, which consist of 1.4 cm thick slabs of POCO AXF-5Q graphite brazed to an Inconel base plate. These tiles are mounted in two concentric bands on the vessel floor, as indicated by the raised sections shown in Fig. 1. Conduction cooling to the water-cooled vessel walls keeps the bulk temperature of the divertor targets below 100°C during normal operation.

A broad range of divertor-region plasma diagnostics is used on DIII-D. Plasma density and electron temperature at the target plates are determined by a radial array of Langmuir probes which span the divertor region. An absolutely calibrated H_α TV camera and several photodiodes with H_α filters are used to measure the radial profiles of neutral hydrogen emission from the divertor plasma. Target-plate surface temperature measurements, which are processed to yield the incident power as a function of space and time, are obtained with a calibrated IR TV camera sensitive in the 8–12 μm wavelength range. In addition, six calibrated ionization gauges measure the neutral molecular density in the divertor, near the plasma midplane, and at the top of the vessel.

II. Plasma Conditions at the Divertor Targets

In this section we document the plasma parameters adjacent to the divertor target plates. Plasma conditions here will determine the longevity of the divertor armor in a fusion reactor since the sputtering and erosion rates increase rapidly with increasing electron temperature, and local heat loads must be maintained at acceptable levels. Conditions at the divertor target are largely determined by the incident power flowing into the scrape-off-layer (SOL). This power flow is itself a function of plasma transport from the core to the edge plasma near the separatrix. A complex interrelationship thus exists between the divertor plasma conditions and the global plasma parameters.

It is known that edge plasma transport is reduced significantly for H-mode discharges [3]. This is evident from measurements of the edge density and temperature profiles at the plasma midplane, shown in Fig. 2. These plots connect data obtained from the Thomson scattering system with that obtained by a moveable Langmuir probe. They show that the edge gradients steepen following the transition from L-mode to H-mode confinement. While 1.5 cm inside the separatrix the density and temperature are higher ($n_e \simeq 7 \times 10^{19}$ m^{-3} and $T_e \simeq 300$ eV) in the H-mode phase,

3

outside the separatrix they are lower ($n_e \simeq 5 \times 10^{18}$ m^{-3} and $T_e \simeq 50$ eV). Thus, power flow to the divertor should be reduced during H-mode since n_e and T_e are lower on the open field lines.

IR TV measurements [4] of the divertor heat flux are consistent with the observed changes in the SOL plasma, as in Fig. 3. At the transition from L-mode to H-mode confinement, the peak power incident on the target plates drops by 20-50%, the location of the peak heat flux shifts closer to the separatrix, and the profile width is reduced from 5-7 cm (1/e full width) to less than 3 cm at the outside intercept for $I_p = 1.2$ MA, $B_T = 2.1$ T, and $\bar{n}_e \simeq 5 \times 10^{19}$ m^{-3}. Since both the peak value and the width of the heat flux profile are reduced in H-mode, the total integrated power deposition ($\int 2\pi r P(r) dr$) drops from the typical L-mode value of 0.3 P_{inj} to approximately 0.1 P_{inj}.

The highest steady-state divertor heat loads are observed during NBI heating with L-mode confinement. Peak power density at the outboard intercept is typically 0.5 MW/m^2 per MW of NBI power, but this may vary by a factor of 2 or more because of measured target plate misalignments of up to 0.3 cm. This peak is displaced radially away from the separatrix intercept by approximately 2 cm. Power deposition at the inboard intercept is considerably lower (≤ 1 MW/m^2) and is displaced from the separatrix by 4-6 cm, as expected from the flux expansion. Integrating over each heat deposition profile shows a factor of 2 to 3 (greater on the outboard intercept) asymmetry in the total power flow. This may be explained by preferential heat loss at the outboard midplane coupled with a longer path length for heat conduction to the inner target plates.

Simultaneous H_α emission and electron temperature measurements also show asymmetries in the divertor plasma during the L-mode phase of NBI. Langmuir probe data indicates that T_e can be about a factor of 2 higher at the outboard intercept than at the inside ($T_e \simeq 15$-20 eV vs $T_e \leq 12$ eV). On the other hand, the H_α emission is frequently brightest at the inside. It is possible to reconcile these asymmetries by assuming that the local heat flux is proportional to the local electron temperature and the ion flux; combining the heat flux measurements with the T_e data then gives similar ion fluxes at each strike point. However, since the ratio of H_α photons/ionization increases as T_e decreases, we expect to see more H_α at the inner separatrix.

4

A more complete picture of the plasma-neutral interactions occurring at the divertor plates is provided by the DEGAS neutral transport code. Using the measured divertor-target power deposition and electron temperature to estimate the neutral source function at the plates (each H^+ produces 0.5 H_2 molecules), it calculates the expected H_α emission and neutral pressures for a typical DIII–D H-mode discharge. We find that the steady-state ($\bar{n}_e \simeq 5 \times 10^{19}$ m^{-3}) can be maintained by high recycling at the divertor plates, so that 86 Torr-l/s of core ionization (ionization within the separatrix) is provided by 8600 Torr-l/s of ionization at the target plates. Comparison of the calculated H_α brightness in the divertor region vs the measured brightness shows agreement to within a factor of 2. Furthermore, the predicted neutral pressures also agree with the measured values, and show that large pressure ratios ($P_{divertor}/P_{midplane} \simeq 10$-$50$) are maintained in the open divertor geometry.

Having characterized the divertor plasma obtained during the quiescent H-mode, some discussion of Edge Localized Modes (ELMs) is now appropriate. In DIII–D two types are observed: giant ELMs, which cause a loss of plasma particles and 10-20% of the stored kinetic energy, and small, so-called "grassy" ELMs which have little directly observable effect on the plasma. Generally, the giant ELMs occur when the NBI power level is well above ($P_{inj} \geq 6$ MW for H^0 into D^+) the H-mode threshold and the gap between the limiter and the separatrix is large (≥ 3 cm).

The effect of an ELM on the edge density and temperature profiles appears in Fig. 4, which shows them before (solid) and after (open) a giant ELM. Little change in the temperature profile is observed, but a substantial loss of edge density has occurred. Profiles obtained during an ELM show that the missing particles have been expelled to the SOL, where rapid parallel loss to the divertor region follows.

The flow of plasma to the divertor region produces increased H_α emission and heat deposition on the target plates. Fig. 5 shows the heat flux at the outer target plates due to a single giant ELM. The heat pulse is very rapid, with a submillisecond rise time and an overall duration of approximately 5 ms. Peak power densities of the order of 50 MW/m^2 are observed, although the power is distributed on a region that is roughly twice as broad as the L-mode case [Fig. 5(b)]. Integration of such heat pulses over space and time [$\int dt \int 2\pi r P(r) dr$] yields total energies which are comparable to that lost from the main plasma.

III. Radiative Losses and Impurity Concentrations

In tokamak plasmas, divertor operation is generally characterized by reduced impurity content and radiative loss compared with similar operation with limiters. During H-mode, however, even relatively clean divertor plasmas ($P_{rad} \leq 0.5\ P_{input}$) are subject to impurity buildup and increased radiative loss, and in some cases [5] this accumulation quenches the H-mode. In contrast to the somewhat discouraging impurity accumulation seen previously at low current on other machines, in DIII–D a favorable scaling of impurity content with plasma current is observed for H-mode discharges with $I_p \geq 1$ MA [6]. That is, the impurity concentration falls with increasing plasma current so that, at the highest currents ($I_p = 2$ MA), it is significantly lower than the L-mode concentrations.

Radiative losses in DIII–D are measured using a bolometer system which consists of an array of 21 detectors that view virtually the entire minor-radius cross section of the plasma from an outboard midplane location. Each channel is collimated to receive radiation from a narrow chord passing through the plasma, as shown in Fig. 6(a), and each detector has sufficient thickness to absorb x-rays with energies up to 10 keV. Detailed measurements of the impurity radiation are provided by three EUV spectrometers: SPRED, an absolutely calibrated multichannel instrument from the Lawrence Livermore National Laboratory that views the plasma tangential to the magnetic axis; STRS, a multichord and multichannel instrument from the Johns Hopkins University with a radial view of the plasma; and GA Technologies MVUV, a multichannel spectrometer with a radial view. At present the impurity concentrations are inferred from MIST-code calculations of the total radiated power and volume-averaged Z_{eff}.

DIII-D has operated with ohmic heating over a wide range of plasma parameters [e.g., $\bar{n}_e = 1\text{–}10 \times 10^{19}$ m^{-3}, $I_p = 0.4\text{–}3.0$ MA, $B_T = 0.8\text{–}2.1$ T]. A typical surface brightness profile appears in Fig. 6(b), which shows that the peak brightness falls on the chord that is centered near the inboard separatrix intercept. Since the radiation from the region near the divertor plates is poloidally asymmetric, only data from the chords in the upper one-half of the vessel are inverted to obtain the radiation density profile within the closed flux surfaces. Over a large ensemble of ohmic divertor shots, the radiation density profiles are characteristically flat to somewhat hollow. The

6

fraction of total radiated power to ohmic input power varies from 0.25 to 0.80, with the highest value corresponding to high density operation ($\bar{n}_e \simeq 4.4 \times 10^{19}$ m^{-3}).

Most of the impurity radiation in ohmic plasmas is the result of C and Ni contamination. Very little oxygen is observed, and its line emission peaks during the initial "burn-through" phase of the discharge. In sharp contrast with the initial divertor results that showed $Z_{eff}^{lim} \simeq Z_{eff}^{div} \simeq 5$–6, present values of Z_{eff} are in the range 1.5 to 2. This cleanup follows the repair of various vacuum leaks.

Radiative losses increase with the addition of NBI heating. Plasmas with L-mode confinement exhibit gross features of the radiated power flux distribution that are very similar to those of ohmic plasmas. Here again the peak surface brightness is coincident with the inner leg of the divertor. However, inversion of the bolometer data from the upper chords yields a radiation density profile which is slightly peaked on axis. Spectroscopic measurements show that while metallic impurities (mainly Ni) account for more than 50% of the radiative loss, the measured $Z_{eff} \leq 2.0$ is due largely to carbon. These impurities apparently do not accumulate during the L-mode phase since the total radiated power remains a constant fraction of the input power after the core plasma density and temperature reach steady-state values. For the L-mode, radiative losses account for approximately 30–40% of the NBI power, with flow to the divertor target plates accounting for another 30%; the remaining 30–40% of the losses are not measured.

Impurity behavior during H-mode operation in DIII–D is complicated by giant ELMs, which periodically cause a loss of more than 30% of the plasma density at large radii ($r/a \geq 0.5$), as can be seen in Fig. 4. These events modulate the brightness of various impurity emission lines as well as the total radiated power. Typical data from a 2.0 MA H-mode discharge with 9.5 MW of NBI power appears in Fig. 7, which shows the temporal evolution of the plasma density, edge H_α emission, the brightness of two emission lines of nickel, and the total radiated power. The effect of the H-mode transition and the ELMs is clearly seen.

At the transition from L-mode to H-mode confinement, the radiative loss drops rapidly back to the ohmic level (data averaged over 16 ms). This is largely the result of a reduction in emission from the divertor region, which follows the drop in power flow to the divertor target plates recorded by the IR TV camera. After this initial

7

drop, the total radiation begins to rise monotonically, only now the profile becomes more and more hollow. Inversion of the data shows a steady decrease in radiation from the divertor region while the power radiated from the outer third of the main plasma increases steadily. Radiation from the core plasma rises more slowly. Just before the first giant ELM occurs, the total radiated power is about 40% of the input power and $Z_{eff} \simeq 1.7$.

The rising impurity radiation observed during the quiescent H-mode has been modeled using an equilibrium solution of the MIST code. Inputs to the code included the measured electron temperature and density profiles and a radial diffusion coefficient for impurities of 1×10^4 cm^2/s. Typical results appear in Fig. 8, which shows a comparison of the calculated radiative loss profiles due to carbon and to nickel with the inverted bolometer profile for a 1.2 MA discharge. Good agreement is obtained.

The picture which emerges from the modeling is that the impurity transport is a strong function of the plasma current during the quiescent period between ELMs. At low current ($Ip \simeq 0.8$ MA), the total electron density and the impurity density profiles are flat and Z_{eff} is relatively high ($\simeq 2.5$). At higher plasma current both profiles become more hollow and Z_{eff} falls as the impurities become more concentrated in the edge plasma. This trend continues up to at least $I_p = 2.0$ MA, where $Z_{eff} \simeq 1.7$. The spectroscopic data are consistent with this picture, as indicated by the data of Fig. 7. It is found that between ELMs, the brightness of the 165 Å line of Ni XVIII (ionization potential of 600 eV) increases linearly, while that of the 118 Å Ni XXV line (ionization potential of 2300 eV) oscillates about an equilibrium value. While the ELM-produced modulation of the Ni XVIII is observed at all values of plasma current, the steady-state brightness of the Ni XXV line drops with increasing plasma current even though the central electron density rises.

IV. Discussion

Operating experience with the single-null open divertor configuration in DIII–D is relevant to planning for next generation tokamak devices such as CIT and ITER. The data from H-mode discharges have implications both for divertor design and for obtaining optimum plasma conditions for ignition. For example, since DIII–D has demonstrated that it is possible to obtain good H-mode confinement ($\tau_E \geq 2\tau_E^{L\text{-mode}}$) with a high recycling (low T_e and high n_e) open divertor, there is little motivation

8

to design a new device with a highly baffled divertor and its accompanying restrictions on possible plasma shapes. The neutral pressure measurements support this conclusion since the divertor/midplane pressure ratio is already large.

Our measurements of the divertor-target heat loads have led us to conclude that the best way to minimize the target heating is to modulate the strike points by sweeping the X-point radial position during the shot. This is preferable to designing highly shaped target plates since we find that the location of the peak heat flux can vary considerably during a shot. The peak moves closer to the separatrix at the onset of NBI and again at the H-mode transition, and its width varies with both NBI power and plasma density. With the onset of so-called locked modes [7], the heat deposition profile has been observed to bifurcate into two peaks situated outside the separatrix intercepts [8]. And during ELMs, when the divertor-target power flux is up to ten times the L-mode value, the energy is deposited over much wider regions. Thus, a dynamic X-point position seems the best way to provide both flexibility in plasma shaping and protection of the target plates themselves.

The choice of graphite for the divertor target plates is motivated by the desire to minimize the impurity influx produced by sputtering. Spectroscopic measurements in JT-60 show much lower impurity levels when using graphite target plates rather than TiC coated molybdenum target plates, although the total radiated power was not limiting plasma operation in either case. In DIII–D, radiative collapse of the H-mode is not observed as it is in both ASDEX (metal targets) and JET (graphite targets), but the radiative losses are increasing throughout the quiescent H-mode phase. The most important factor in controlling the impurity influx is to maintain a low electron temperature at the target plates so that the ion impact energy ($\simeq 3\ T_e$) is below the threshold for sputtering. A related issue, which still needs resolving, is that of the effect of the apparent inboard/outboard asymmetry in the electron temperature at the target plates. This asymmetry may produce nonuniform surface erosion with subsequent material migration within the divertor region.

The lower radiative losses observed in DIII–D are also a consequence of operating at high plasma currents. As shown above, a favorable scaling of impurity content with plasma current is obtained. We believe that this is a result of the edge-peaking of the density profile observed with increasing plasma current, so that impurities are confined to the edge plasma. This not only directly reduces the core impurity content,

but allows ELMs, which produce a loss of the edge plasma, to more efficiently remove impurities from within the closed flux surfaces to the open field lines in the scrape-off-layer. This suggests that an optimal H-mode plasma with minimal radiative losses may be one in which the density profile is slightly hollow and which has some low level of ELM activity to serve as an impurity pumping mechanism.

Acknowledgments

The data presented in this document have been presented previously as a GA Technologies Report GA-A19101.

REFERENCES

1. K.H. Burrell et al., Phys. Rev. Lett. **59**, 1432 (1987).

2. J. Luxon et al., Plasma Phys. Cont. Nucl. Fus. Research 1986 (Proc. 11 Int. Conf. Kyoto, Japan, 1986), Vol. 1, IAEA, Vienna (1987) 1711.

3. F. Wagner et al., Phys. Rev. Lett. **53**, 1453 (1984).

4. D.N. Hill et al., submitted to Nucl. Fusion.

5. E.R. Müller et al., Max-Planck-Institut für Plasmaphysik Report IPP III/112, 1986.

6. N.H. Brooks et al., in preparation for Phys. Rev. Lett.

7. A. Kellman et al., Bull. Am. Phys. Soc. **32**, 1846 (1987).

8. D.N. Hill et al., Bull. Am. Phys. Soc. **32**, 1898 (1987).
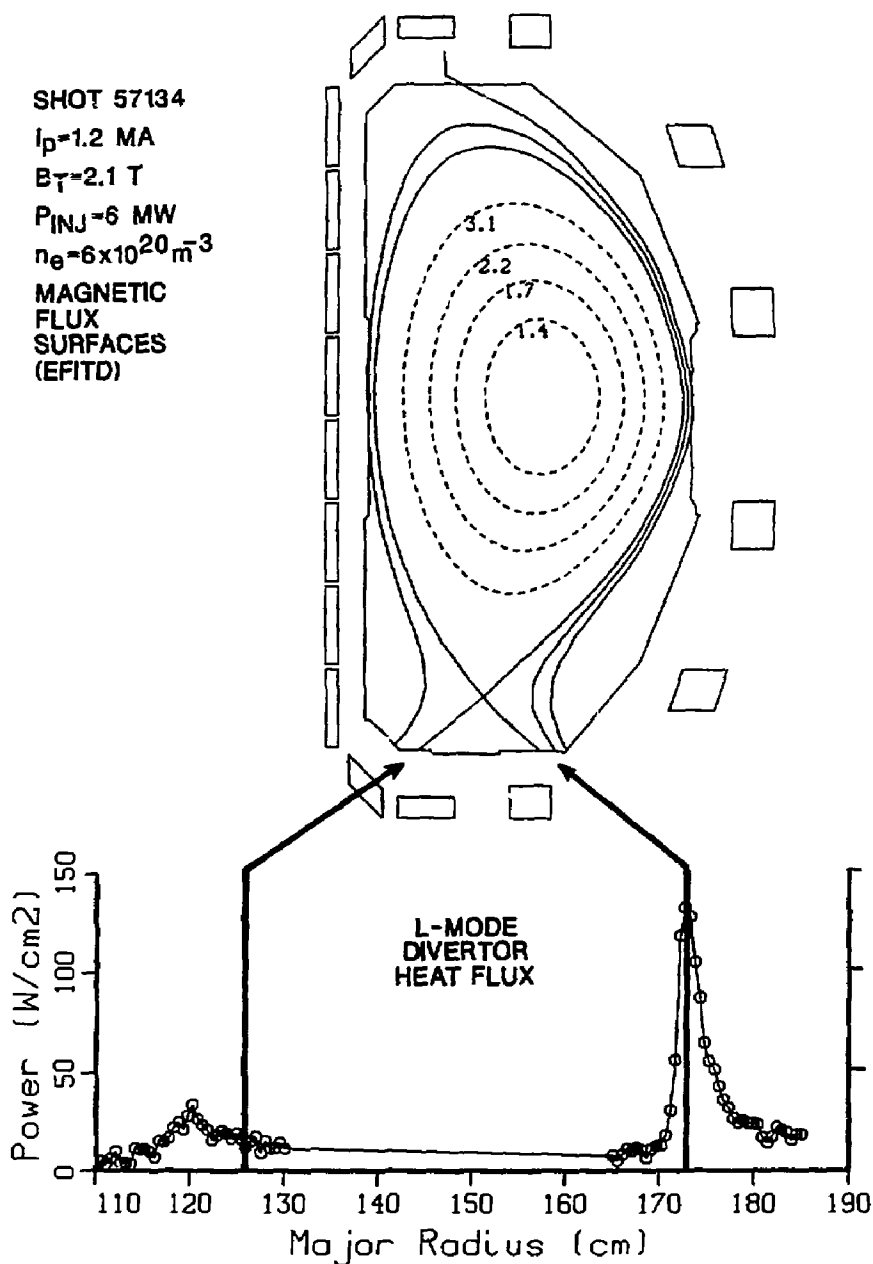
Fig. 1. Cross section of the DIII-D vessel showing magnetic flux surfaces and measured heat-flux distribution on the divertor-target plates.

12
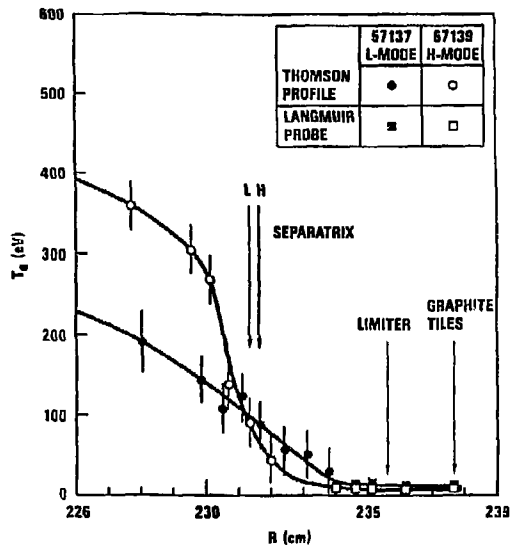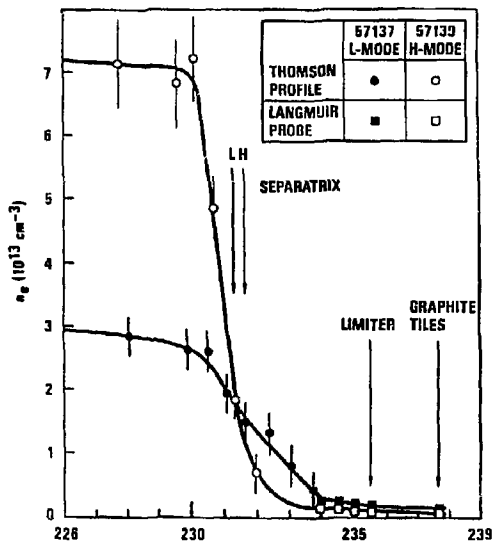
Fig. 2. Measured electron temperature and density profiles at the plasma midplane.

SHOT 56512
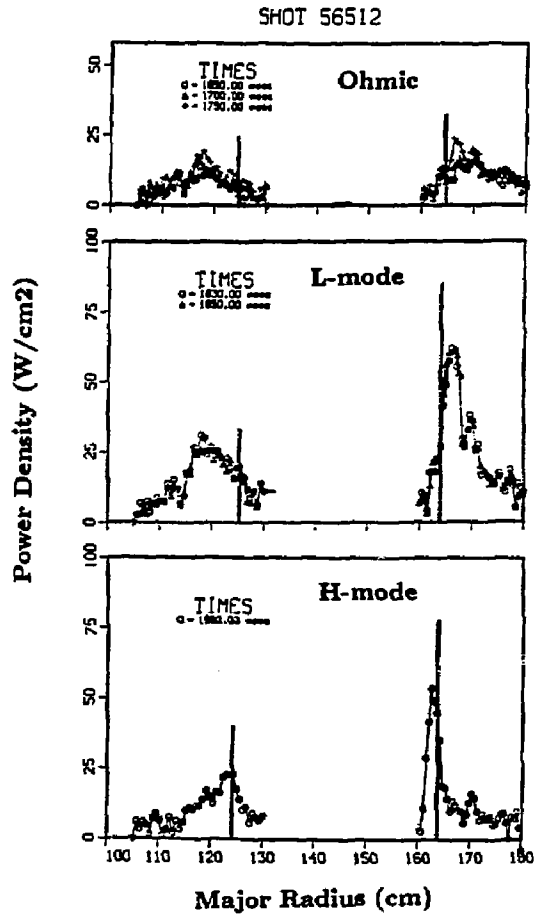
Fig. 3. Measured divertor-target power deposition profiles.
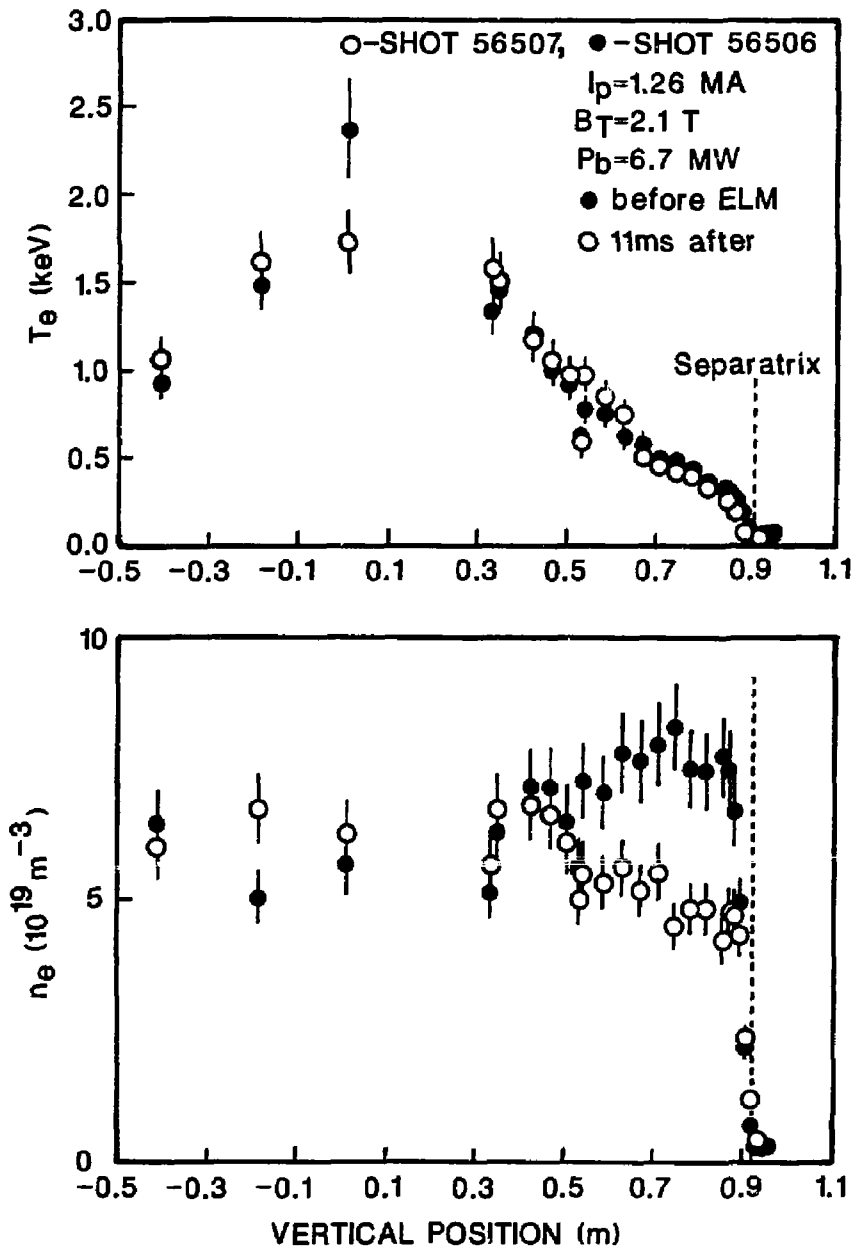
EFFECT OF ELMS ON THOMSON PROFILES

O-SHOT 56507, •-SHOT 56506

I_p=1.26 MA
B_T=2.1 T
P_b=6.7 MW
• before ELM
O 11ms after

Separatrix

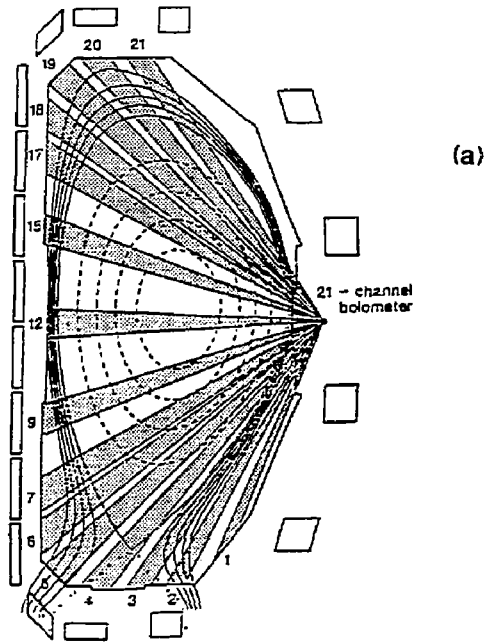Fig. 4. The effect of a giant ELM on the edge electron density and temperature.

15
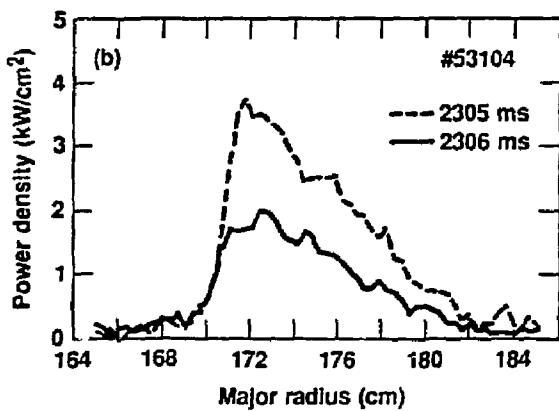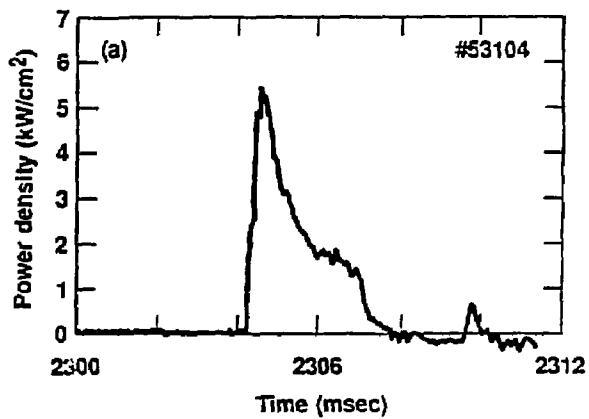
Fig. 5. Heat flux at the outer divertor-target plates due to a giant ELM: (a) Peak power density vs time; (b) Power density profile at the times indicated.

16

(a)

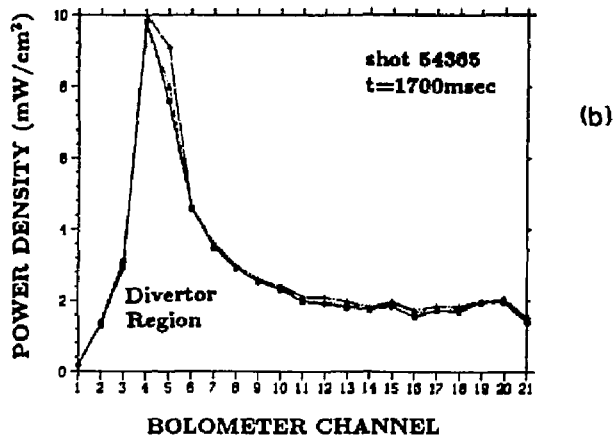**SURFACE RADIATION DISTRIBUTION**

(b)

Fig. 6. Measurements of the total radiated power: (a) Field-of-view of the 21 channel bolometer array; (b) Typical surface brightness profile for an ohmically heated plasma.
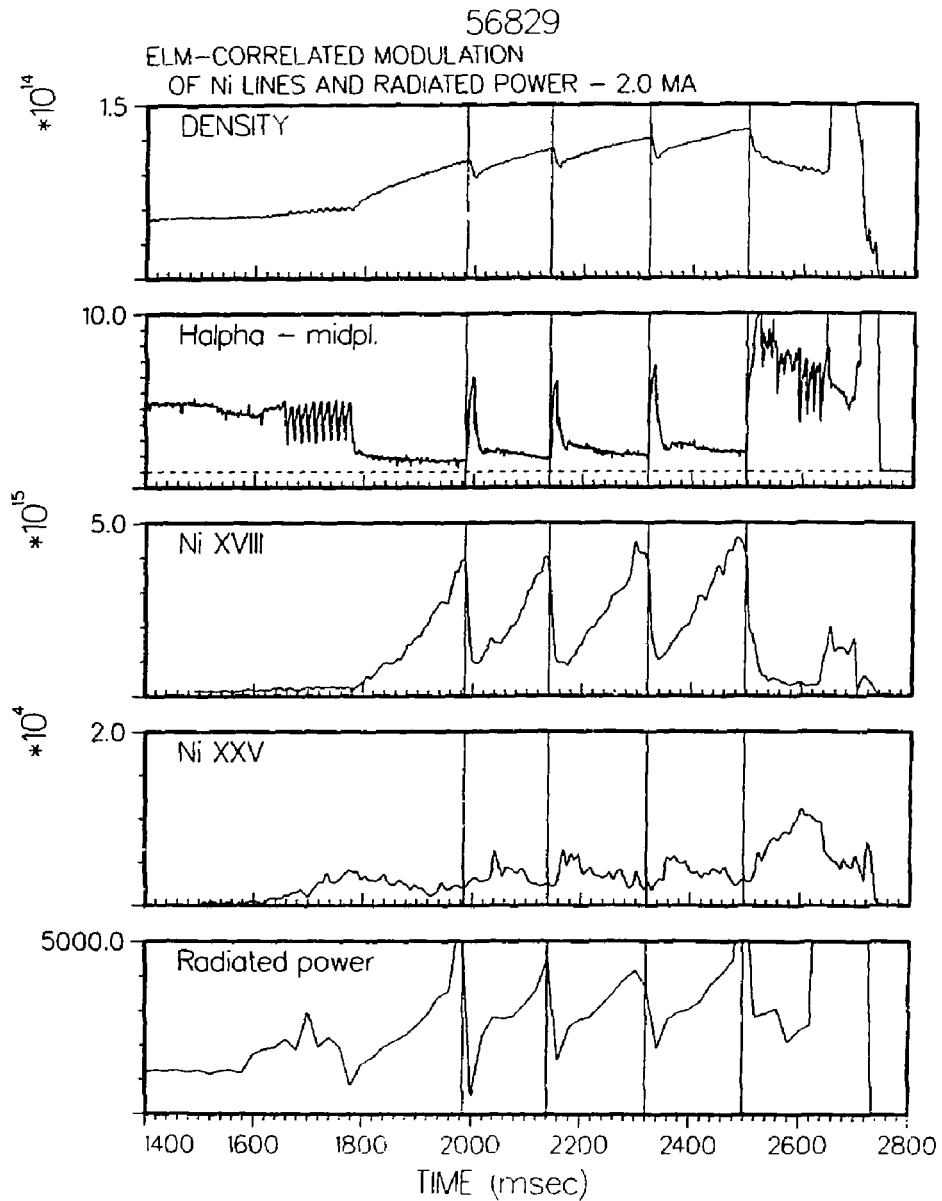
17

56829

ELM-CORRELATED MODULATION
OF Ni LINES AND RADIATED POWER - 2.0 MA

Fig. 7. Typical data from a high current H-mode discharge showing the temporal behavior of the (top to bottom) plasma density, midplane H_α brightness, Ni XVIII brightness at 165 Å, Ni XXV brightness at 118 Å, and the total radiated power.
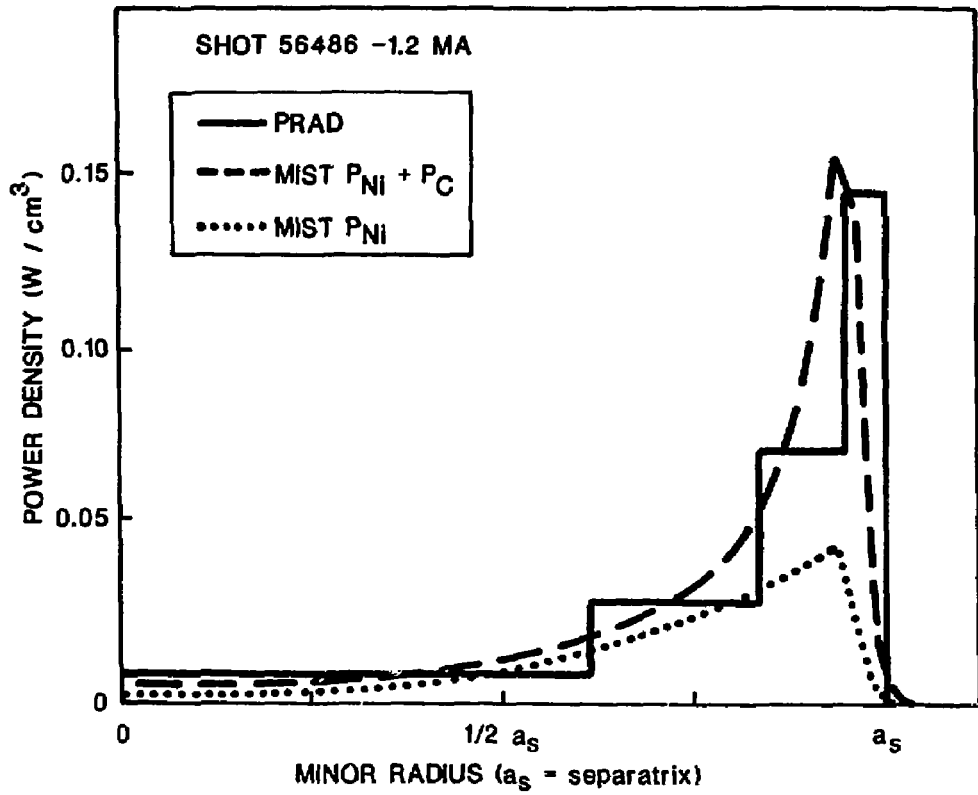
RADIAL PROFILES OF RADIATIVE LOSS

Fig. 8. Comparison of MIST-code calculations of impurity radiation profiles with an inversion of the bolometer profile of total radiation.